Optimizing the Performance of Single-Phase Photovoltaic Inverter using Wavelet-Fuzzy Controller

Khan, Mohammed Ali; Haque, Ahteshamul; Kurukuru, Varaha Satya Bharath; Blaabjerg, Frede

Published in:
e-Prime - Advances in Electrical Engineering, Electronics and Energy

DOI (link to publication from Publisher):
10.1016/j.prime.2022.100093

Publication date:
2023

Document Version
Publisher's PDF, also known as Version of record

Electrical Power and Energy Systems 148 (2023) 108952

Contents lists available at ScienceDirect

International Journal of Electrical Power and Energy Systems

journal homepage: www.elsevier.com/locate/ijepes

Fault current control of MMC in HVDC-connected offshore wind farm: A coordinated perspective with current differential protection

Guoqing Gao [a,*], Heng Wu [a], Frede Blaabjerg [a], Xiongfei Wang [b]

[a] Department of Energy, Aalborg University, Aalborg, Denmark
[b] Division of Electric Power and Energy Systems, KTH Royal Institute of Technology, Stockholm, Sweden

ARTICLE INFO

Keywords:
Current differential protection
Offshore wind farm
Coordinated control
Short-circuit fault
MMC

ABSTRACT

The modular multilevel converter (MMC) based high-voltage dc (HVDC)-connected offshore wind farm (OWF) is power electronic converter dominated power system, where the conventional current differential protection may not operate effectively. Based on the basic operation principle of the current differential relay, this paper points out that the phase difference (ϕ_{diff}) of fault currents from MMC and OWF should be limited within a specific range, i.e. ($-\phi_{diffmax}$, $\phi_{diffmax}$), to guarantee the reliable tripping of the current differential relay. Yet, the highly control-dependent fault currents from the MMC and OWF could yield an arbitrary ϕ_{diff} that might beyond ($-\phi_{diffmax}$, $\phi_{diffmax}$), which leads to the possible malfunction of the current differential relay. To tackle this challenge, the coordinated control method of MMC is proposed to align the phase angle of its fault current with that of the OWF, such that $\phi_{diff} \in (-\phi_{diffmax}, \phi_{diffmax})$ can be always guaranteed, so as the reliable operation of the current differential relay. Finally, the proposed coordinated control is verified by the electromagnetic transient (EMT) simulations in PSCAD and the real-time digital simulator (RTDS).

1. Introduction

In recent years, offshore wind farms (OWFs) are extensively constructed and connected to the power grid through the modular multilevel converter (MMC) based high-voltage dc (HVDC) transmission systems. The OWF-HVDC system is power electronic converters dominated, which features high controllability and operational flexibility [1,2]. Thus, the fault currents of OWF and HVDC system are highly dependent on their control strategies, which is essentially distinct from the fault characteristics of synchronous generators (SGs). This difference significantly challenges the efficacy of conventional current differential protection which is designed based on fault current characteristics of SGs.

The fault currents of SGs are dependent on the electromagnetic dynamics of electrical machines as well as the external faulty network, which features:

1) The high ($\geq$3p.u.) magnitude fault current, which is usually significantly higher than the nominal current.
2) The fault current is highly inductive [3].
3) Significant negative- and zero-sequence current can be provided for unbalanced faults.

Different from SGs, the fault current responses of converters are highly dependent on their control strategies, which features:

1) The low magnitude ($\leq$1.5p.u.) fault current, which is generally dependent on the thermal limit of power semiconductor devices.
2) The phase angle of the fault current is highly controllable and usually mandated by the grid code. Besides, it is also affected by the manufacturer specific and the proprietary control system [4].
3) The zero-sequence current of grid-connected converters is commonly suppressed. The injection of negative-sequence current is not commonly required, with a few exception, e.g., German grid code [5].

The highly controlled fault current from converters has significant adverse effect on the efficacy of different kinds of protection relays [6]. Boasting the 100 % selective [7], the current differential protection is regarded as the last line of defence for the power electronic converter dominated power system when other conventional protections might

* Corresponding author.
E-mail address: gga@energy.aau.dk (G. Gao).

https://doi.org/10.1016/j.ijepes.2023.108952
Received 26 August 2022; Received in revised form 30 November 2022; Accepted 3 January 2023
Available online 17 January 2023

fail. The performance of current differential protection in the system where power converters (like PV or wind farm) are connected to the passive network is investigated in [8,9]. It is pointed out that current differential protection remains reliable provided the ac grid is strong. It is because the magnitude of fault current from the stiff ac grid outweighs that of the PV/wind farm, such that enough differential current can always be generated regardless of the fault current characteristic of PV/wind farm. However, the sensitivity of the current differential protection is degraded when the ac grid becomes weaker with the reduced fault current infeed [10]. It comes to the worst scenario where the passive grid is replaced by the converter, such that both terminals of the transmission line are fed by converters with limited fault current infeed, e.g., OWF-HVDC system considered in this work. As will be demonstrated in this paper, the insufficient differential current might be yielded due to the limited fault current infeed from both OWF and HVDC provided their phase angle difference is beyond the specific range, which leads to the malfunction of the current differential protection.

There are currently two research directions to tackle the protection challenges for the converters-dominated system like the OWF-HVDC. The first emerging research direction is to adopt the new protection principles that are independent of source characteristics. The time domain and traveling-wave protection [11] are not sensitive to the source characteristics or load condition, but based on the response to the fault point excitation related with the fault location. Therefore, the fast response of the traveling-wave protection is tailored to the HVDC transmission lines protection. However, in the offshore ac grid with multiple terminals connected with wind farm clusters, the traveling-wave protection encounters many challenges, e.g. faulty-segment identification due to the reflections of the first incident wave from different points [12]. Besides, the protection principles based on the parameter and topology characteristics identification of the network with the measured variables are weakly correlated with source characteristics. The work in [13–15] proposed the Pearson correlation and cosine similarity based protection principles for ac lines connecting SGs and wind farm, which are independent of the control strategies of wind farm converters. However, both sides of the ac lines are power converters in OWF-HVDC system, the fault current characteristic of which is quite complex due to the control flexibility of MMC. As a result, these protection methods based on similarity or correlation coefficient have risk of malfunction with the internal fault in the presence of MMC station [16] of the OWF-HVDC system.

The second research direction evolves from passive protection to the active protection, the latter can be realized either by actively injecting signals to facilitate fault detection, or by actively controlling the fault characteristics of power converters to get coordinated with traditional protections. The active protection based on signal injection would inject the specially designed test signals and measure the corresponding response to recognize the fault condition [17,18]. Yet, the test-signal injection method encounters a lot of challenges, e.g. the selection and generation of the injection signal, the selection of injection moment, the processing of the detected signals, etc [19]. However, the active protection based on the coordination with converter control is compromising considering that the fault characteristics are highly controlled by converters. For the OWF-HVDC system, although the magnitude of the fault current from MMC should be limited to protect the switching devices, its phase angle can be controlled to an arbitrary value. This provides a degree of freedom that can be utilized to improve the efficacy of current differential protection.

In this paper, the coordinated fault current control of MMC is proposed. By actively controlling the phase angle of the fault current of MMC to make it aligned with that of the OWF, the reliable operation of current differential protection is guaranteed. The benefits of the proposed method are threefold: 1) It does not require any modifications on the traditional current differential protection algorithm, which simplifies the field implementation. 2) The proposed method is solely based on the unused control freedom of the MMC, i.e., the phase angle of its fault current, such that it does not contradict with existing control objectives of the OWF-MMC system. 3) The communication between OWF and MMC is not required after the fault onset, which avoids the communication delay and improves the relay speed.

The rest of the paper is organized as follows. Section II elaborates the system structure and the characteristics of the controlled fault current from both MMC and OWF. Then, the impact of controlled fault current on the efficacy of the current differential protection relay is discussed in Section III and IV. It is revealed that the arbitrary phase difference of fault currents from MMC and OWF might lead to the malfunction of current differential protection. To tackle this challenge, the coordinated control method of MMC is proposed to align the phase angle of its fault current with that of the OWF in Section V, such that the reliable operation of the current differential protection can be guaranteed. Finally, the proposed coordinated control is validated through the electromagnetic transient (EMT) simulation in Section VI and the experimental setup based on RTDS in Section VII.

2. System description

Fig. 1 illustrates the system diagram of OWF-HVDC. The offshore ac grid is a converters-dominated system, where the grid-side voltage-source converters (VSCs) of wind turbines are connected through submarine cables to the MMC-HVDC station. MMC adopts the grid-forming (GFM) control [20] to provide the voltage and frequency reference for the offshore ac grid, while the grid-following (GFL) control [21] is adopted in the grid-side VSCs of wind turbines in this study.

The control schematic of the OWF-HVDC is depicted in Fig. 2. For simplicity, the OWF is aggregated as a single GFL-VSC, where a typical vector current control is used to control its output current (i_{wd}, i_{wq}) to follow the current reference (i^*_{wd}, i^*_{wq}). The terminal voltage v_w is measured for synchronizing the GFL-VSC with the ac system by means of the phase-locked loop (PLL). In the event of a short-circuit fault, the output current reference i^*_{wqf} of VSC is switched to the fault mode according to the fault ride-through requirement: the reactive current injection of VSC follows the grid code [22] as shown in Fig. 3, which is a tabulated function of the magnitude of the terminal voltage, i.e.,

$$i^*_{wqf} = \begin{cases} 0 & if\ v_w > 0.9\ \text{p.u.} \\ 2(v_w - 1) & if\ 0.5\ \text{p.u.} < v_w \leqslant 0.9\ \text{p.u.} \\ -1 & if\ v_w \leqslant 0.5\ \text{p.u.} \end{cases} \tag{1}$$

Accordingly, the reference of the injected active current can be calculated as

$$\left|i^*_{wdf}\right| = \sqrt{I^2_{W\text{lim}} - \left|i^*_{wqf}\right|^2} \tag{2}$$

where $I_{W\text{lim}}$ represents current limit of the GFL-VSC.

On the other hand, the GFM control system of MMC consists of an outer voltage loop and an inner current loop, as shown in Fig. 2. To avoid the overcurrent of MMC, the current limiter is inserted at the output of the outer-loop voltage controller. After the inception of a low-impedance short-circuit fault at the ac interconnection between the MMC and the OWF, the terminal voltage drop of MMC will lead to the increase of the voltage regulator output (i.e., the fault current references i^*_{md} and i^*_{mq}) until the current limiter is activated, with which, the

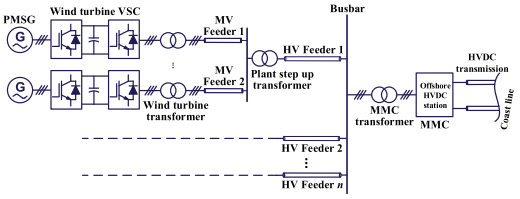

Fig. 1. System diagram of the HVDC-connected OWF.

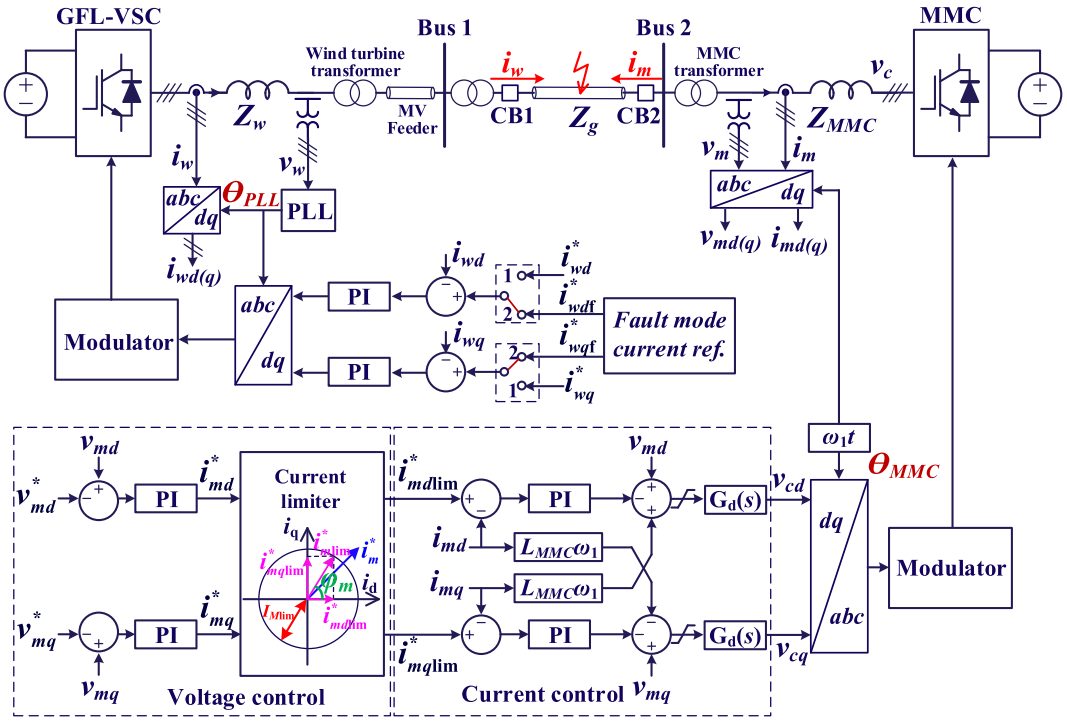

Fig. 2. Schematic of the HVDC-connected OWF.

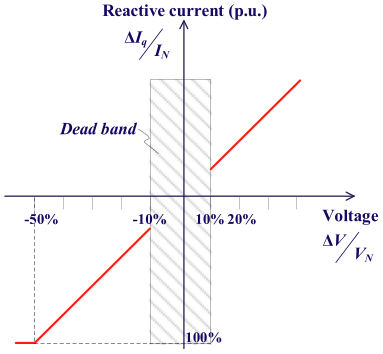

Fig. 3. The additional required reactive current during voltage excursions (V_N: the nominal terminal voltage of VSC; I_N: the nominal output current of VSC; ΔV: the terminal voltage excursion of VSC; ΔI_q: the additional required reactive current of VSC).

magnitude of the fault current from MMC is limited to its current rating, i.e., $I_{M\text{lim}}$.

It is worth mentioning that there are two dq frames in the OWF-MMC system. One is the OWF dq frame that is defined by the output phase angle of the PLL, i.e., θ_{PLL}, and the other is the MMC dq frame whose phase angle is the integration of the fundamental frequency (ω_1), i.e., $\theta_{\text{MMC}} = \omega_1 t$. Fig. 4 shows the phasor diagram of fault currents of the OWF and the MMC, where subscripts w and m represent the variables in the OWF-dq frame and MMC-dq frame, respectively. It is known from Fig. 4 that the phase difference between fault currents of the OWF and the MMC can be calculated as

$$\phi_{diff} = \delta + \varphi_m + \varphi_w \tag{3}$$

where δ is the phase difference between the two dq frames, i.e.,

$$\delta = \theta_{MMC} - \theta_{PLL} \tag{4}$$

φ_w and φ_m are phase angles of the fault currents from GFL-VSC and MMC in respect to their own dq frames. Specifically, φ_w and φ_m as

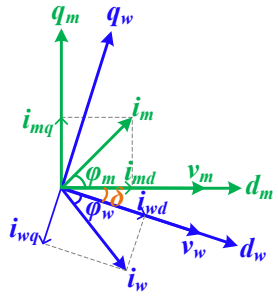

Fig. 4. Phasor diagram of the fault currents from MMC and wind farm.

expressed as (5) and (6), are the phase angles that i_w lags d_w axis and i_m leads d_m axis, respectively.

$$\varphi_w = -\arctan\left(\frac{i_{wq}}{i_{wd}}\right) \tag{5}$$

$$\varphi_m = \arctan\left(\frac{i_{mq}}{i_{md}}\right) \tag{6}$$

It is known from (1) and (2) that the active and reactive current injection of OWF is clearly specified by the grid code, so as to φ_w. Yet, there is no grid code requirement on φ_m, such that it can be controlled to an arbitrary value [23], which leads to an arbitrary ϕ_{diff}. As will be discussed in the following sections, the value of ϕ_{diff} has a significant impact on the efficacy of current differential protection.

3. Control impacts on efficacy of current differential protection

The current differential protection is the main protection for high-voltage (HV) feeders and busbars in OWF [24]. Considering the fault current characteristics in OWF-HVDC are different from that of the conventional SGs dominated system, this part will introduce the basic principles of current differential protection for feeders and busbar, then

investigate the impact of converter control on the efficacy of current differential protection.

3.1. Basic operation principle

The current differential protection is based on the Kirchhoff's Current Law (KCL). The basic principle of the current differential protection can be illustrated in Fig. 5, where the SGs are connected through a feeder. The current differential protection will collect the current information $\dot{I}_s$ and $\dot{I}_r$ of both sides of the protected feeder. If the currents from bus to feeder is defined as positive, the sum of the currents from both sides of the protected feeder is equal to zero for external fault or normal condition, yet much greater than zero for internal fault as shown in Fig. 5(a)(b). Therefore, the current differential protection can easily differentiate the internal fault from the external fault or normal condition according to their distinct current characteristics.

However, due to the transformation errors of the current transformer (CT) or the capacitive charging current in practical applications as shown in Fig. 5(c), the sum of the currents from both sides of the protected feeder is no longer exactly equal to zero for external fault. As a result, the ideal current differential protection based on KCL to distinguish between the internal and external faults as illustrated in Fig. 5(a)(b) may fail in practical applications. Therefore, the restraint current $I_{Res} = \left|\dot{I}_s - \dot{I}_r\right|$ is utilized in the practical current differential protection operation criterion [7]:

$$\begin{cases} I_{Op} > kI_{\mathrm{Res}} \\ I_{Op} > I_{op[0]} \end{cases} \tag{7}$$

where $I_{Op} = \left|\dot{I}_s + \dot{I}_r\right|$ is the differential current. $I_{\mathrm{op}[0]}$ is the threshold value to avoid the mal-operation when I_{Res} is close to zero. The coefficient k is the bias factor [7], which defines the slop of the operating characteristic and is typically set as 0.8 for feeder protection of OWF. The relay operation criterion of (7) can be illustrated in Fig. 6 corresponding to the operate area above the relay operation characteristic. The relay of the current differential protection will trip if the criterion (7) is satisfied, e.g. point A.

3.2. Efficacy analysis

3.2.1. Busbar protection

As shown in Fig. 7, the currents of n HV feeders are collected on the busbar and then flow to the MMC. The capacity of the offshore wind farm S_{OWF} is the sum of the n wind farm clusters. For simplicity, it is assumed that the parameters of the n wind farm clusters are identical such that they can contribute similar fault currents.

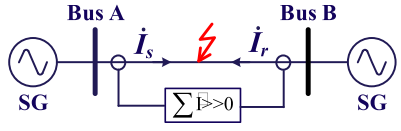

(a) Internal fault (the fault within the protected range)

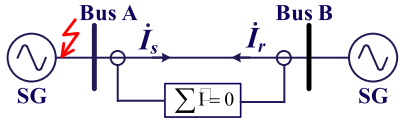

(b) External fault (the fault beyond the protected range)

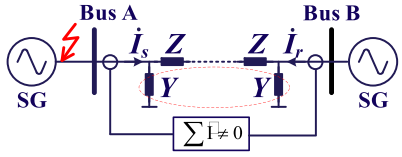

(c) External fault with capacitive charging current

Fig. 5. Basic principle of current differential protection.

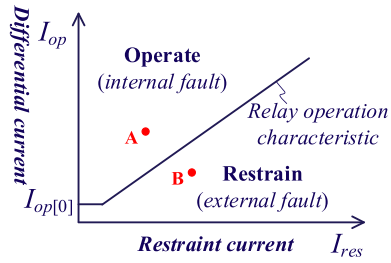

Fig. 6. I_{Op}/I_{Res}-diagram of the differential protection.

In the event of a short-circuit fault on busbar, the fault currents contributed from the OWF side can be calculated as $\dot{I}_{w1} + \dot{I}_{w2} + \cdots + \dot{I}_{wn} = n^*\dot{I}_w$, while the fault current injected by the MMC is denoted as $\dot{I}_m$. Therefore, the differential and restraint currents can be calculated as

$$\begin{aligned} I_{Op} &= \left|\dot{I}_m + \dot{I}_{w1} + \dot{I}_{w2} + \cdots + \dot{I}_{wn}\right| = \left|\dot{I}_m + n\dot{I}_w\right| \\ I_{Res} &= \left|\dot{I}_m\right| + \left|\dot{I}_{w1}\right| + \left|\dot{I}_{w2}\right| + \cdots + \left|\dot{I}_{wn}\right| = \left|\dot{I}_m\right| + n\left|\dot{I}_w\right| \end{aligned} \tag{8}$$

Define r as the capacity ratio between the MMC and OWF ($S_{\mathrm{MMC}}/S_{\mathrm{OWF}}$), i.e., $\left|\dot{I}_m\right| = r^*n^*\left|\dot{I}_w\right|$, with ϕ_{diff} as the phase difference between $\dot{I}_m$ and $\dot{I}_w$, (8) can be rewritten as (9) according the law of cosines.

$$\begin{aligned} I_{Op} &= \left|\dot{I}_m + n\dot{I}_w\right| = \frac{\sqrt{r^2 + 2r\cos\phi_{diff} + 1}}{r}\left|\dot{I}_m\right| \\ I_{Res} &= \left|\dot{I}_m\right| + n\left|\dot{I}_w\right| = \frac{r+1}{r}\left|\dot{I}_m\right| \end{aligned} \tag{9}$$

Substituting (9) into the operation criteria of the current differential relay given by (7), which yields

$$\sqrt{r^2 + 2r\cos\phi_{diff} + 1} > k(r+1) \tag{10}$$

Eq. (10) should hold to guarantee the successful tripping of the current differential relay in the event of a short circuit fault. Accordingly, the acceptable range of ϕ_{diff} in respect to r can be calculated, and the results are given in Fig. 8. It can be noticed that the current differential relay can trip with arbitrary ϕ_{diff} provided $S_{\mathrm{MMC}} \gg S_{\mathrm{OWF}}$, e.g., $r > 9$. This is understandable since the differential current would be dominated by the I_m in this scenario such that the impact of ϕ_{diff} is limited. Yet, in practice the MMC usually has similar or slightly larger capacity compared with that of OWF, i.e., $1 < r < 2$. In this case, the differential current will be highly affected by ϕ_{diff}. As shown in Fig. 8, $\phi_{diff} > 75°$ would lead to the malfunction of the current differential relay when $r = 1.2$.

3.2.2. Feeder protection

In the event of a short circuit fault on feeder 1 as illustrated in Fig. 9, the fault current flowing from the wind farm cluster 1 to the fault location is denoted as $\dot{I}_{w1}$, while the fault current flowing from the busbar to the fault location is denoted as $\dot{I}_{sum}$, which is contributed by the fault currents of the MMC and other wind farm clusters as expressed below:

$$\dot{I}_{\mathrm{sum}} = \dot{I}_m + \dot{I}_{w2} + \cdots + \dot{I}_{wn} \tag{11}$$

Therefore, the differential current I_{Op} and the restraint current I_{Res} of the current differential relay on feeder 1 can be calculated as

$$\begin{aligned} I_{Op} &= \left|\dot{I}_{w1} + \dot{I}_{sum}\right| = \left|\dot{I}_m + n\dot{I}_w\right| \\ I_{Res} &= \left|\dot{I}_{w1}\right| + \left|\dot{I}_{\mathrm{sum}}\right| = \left|\dot{I}_w\right| + \left|\dot{I}_m + (n-1)\dot{I}_w\right| \end{aligned} \tag{12}$$

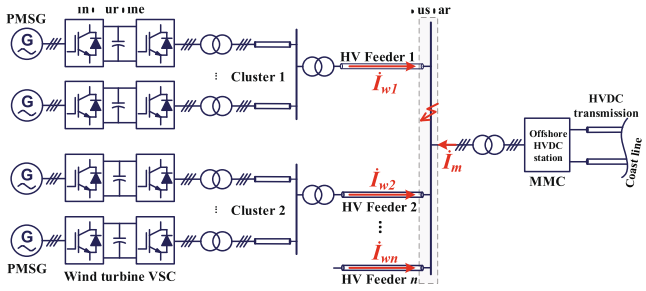

Fig. 7. System diagram of the OWF-MMC system with short-circuit fault on busbar.

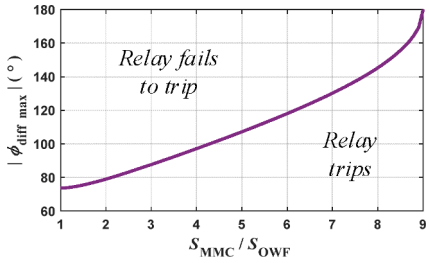

Fig. 8. The maximum phase difference between $\dot{I}_m$ and $\dot{I}_w$ that the relay of current differential protection for busbar can trip.

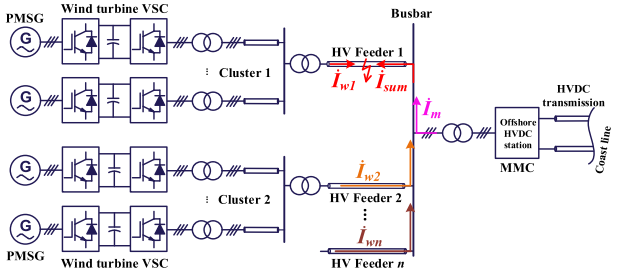

Fig. 9. System diagram of the OWF-MMC system with short-circuit fault on HV feeder 1.

Define r as the capacity ratio between the MMC and OWF (S_{MMC}/S_{OWF}), i.e., $|\dot{I}_m| = r^*n^*|\dot{I}_w|$, with ϕ_{diff} as the phase difference between $\dot{I}_m$ and $\dot{I}_w$, (12) can be rewritten as

$$I_{Op} = \frac{\sqrt{r^2 + 2r\cos\phi_{diff} + 1}}{r}|\dot{I}_m|$$
$$I_{Res} = \frac{\sqrt{(n-1)^2 + r^2n^2 + 2rn(n-1)\cos\phi_{diff}} + 1}{rn}|\dot{I}_m| \quad (13)$$

Substituting (13) into the operation criteria of the current different relay given by (7), which yields

$$n\sqrt{r^2 + 2r\cos\phi_{diff} + 1} > k\left(\sqrt{(n-1)^2 + r^2n^2 + 2rn(n-1)\cos\phi_{diff}} + 1\right) \quad (14)$$

Eq. (14) should hold to guarantee the successful tripping of the current differential relay in the event of a short circuit fault on HV feeder. Accordingly, the acceptable range of ϕ_{diff} (hereinafter also referred to as safe phase difference range) in respect to the capacity ratio r and the number of HV feeders n can be calculated, and the results are given in Fig. 10. It can be noticed that the safe phase difference range (SPDR) expands when increasing n for the common capacity ratios in practice, i.e., $1 < r < 2$. If $n = 8$ and $r > 2$, the maximum ϕ_{diff} that the relay can successfully trip increases to 180°, which means the SPDR reaches the maximum value and the phase difference between $\dot{I}_w$ and $\dot{I}_m$ has no adverse effect on the operation of relay. Besides, it can be noticed by comparing Fig. 8 and Fig. 10 that the current differential protection for busbar can be regarded as the special case of the current differential protection for HV feeder with only one wind farm cluster, thus the number of HV feeders has no effect on SPDR of the busbar protection.

The current differential protection is designed based on the characteristic that the fault current direction of both sides of the protected line is similar. However, the phase angle φ_w of the fault current $\dot{I}_w$ from wind turbine VSC is determined by the grid code on low-voltage ride-through. The phase angle φ_m of the fault current $\dot{I}_m$ from MMC can be controlled to an arbitrary value. Therefore, the phase difference ϕ_{diff} of the fault currents from wind turbine VSC and MMC is determined by the converter control. If ϕ_{diff} is large enough to exceed the SPDR, the criterion of (7) could not be satisfied after fault inception, then the relay fails to trip.

4. Challenges of the current differential protection

As mentioned before, ϕ_{diff} has a significant impact on the efficacy of the current differential protection. Therefore, in this section, the dynamics of ϕ_{diff} will be characterized to assess the risk of exceeding SPDR in the OWF-MMC system. It is known from (3) that ϕ_{diff} is contributed by δ, φ_w and φ_m, which is determined by the fault current references settings, current loop dynamics as well as PLL dynamics. Since the timescale of the current control (around several ms) is much smaller than the operation time of the current differential relay (around 1 ~ 2 fundamental cycles), an ideal current reference tracking can be assumed. Yet, the dynamics of the PLL should be considered when analyzing the dynamics of ϕ_{diff} at 1 ~ 2 fundamental cycles due to its much slower dynamics (around 100 ms) [25].

Fig. 11 shows the equivalent circuit diagram of the OWF-HVDC as illustrated in Fig. 2 with a symmetrical 3-phase-to-ground fault on the HV cable feeder with PLL dynamics considered, where R_f, Z_g, and Z_2 are the fault resistance, HV feeder impedance, and the equivalent impedance of the MMC transformer, respectively. Z_1 is the equivalent impedance of the MV feeders, wind turbine transformers, and the plant

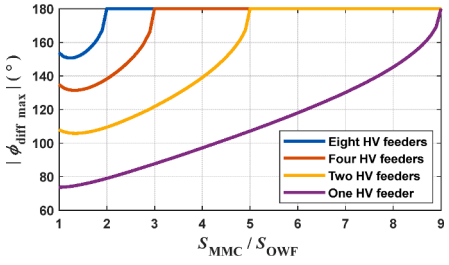

Fig. 10. The maximum phase difference between $\dot{I}_m$ and $\dot{I}_w$ that the relay of current differential protection can trip.

step-up transformers. f_1 is the fault location on the HV feeder, which is determined by a ($0 \le a \le 1$). The relay of the current differential protection will utilize the measured current information of both ends of the protected HV feeder, then trip after fault inception according to the criteria of (7).

MMC-connected OWF involves two synchronous reference frames for wind turbine VSC and MMC, respectively. The wind turbine VSCs are synchronized with the PCC voltage through PLL. As a result, the d-axis phase angle of the synchronous reference frame of the wind turbine VSC is θ_{PLL}, which equals to the phase angle of the PCC voltage during steady state. Accordingly, the current phase angle φ_w of VSC can be controlled relative to the PCC voltage to distribute the injected active and reactive current.

The PLL is a feedback system, the block diagram of which is shown in Fig. 12. The input is the three-phase PCC voltage of VSC, which is transformed to the dq frame. The q-axis voltage v_{wq} is regulated via a PI controller to track the phase angle of PCC. The output phase angle θ_{PLL} of the PLL can be expressed as

$$\theta_{PLL} = \int \omega_{PLL} \mathrm{d}t \tag{15}$$

where

$$\begin{cases} \omega_{PLL} = \omega_1 + \Delta\omega_{PLL} \\ \Delta\omega_{PLL} = K_p v_{wq} + K_i \int v_{wq} \mathrm{d}t \end{cases} \tag{16}$$

ω_1 is the nominal frequency. K_p and K_i are the proportional and integral coefficient of the PI controller, respectively.

MMC adopts the grid-forming control to provide the voltage and frequency reference for the offshore ac grid according to its own synchronous reference frame. The phase angle of the terminal voltage of MMC can be expressed as:

$$\theta_{MMC} = \int \omega_1 \mathrm{d}t \tag{17}$$

Besides, the d-axis of the synchronous reference frame of MMC is aligned with the terminal voltage. Thus, the fault current phase angle φ_m of MMC can be controlled relative to the d-axis of its synchronous reference frame.

Substituting (15) and (17) into (4), the phase difference δ between the two dq frames can be expressed as:

$$\begin{aligned} \delta &= \theta_{MMC} - \theta_{PLL} \\ &= \int \left(- K_p v_{wq} - K_i \int v_{wq} \mathrm{d}t \right) \mathrm{d}t \end{aligned} \tag{18}$$

Since there are two synchronous reference frames in OWF-MMC system as illustrated in Fig. 4, the relationship of the fault current from MMC represented in different reference frames can be expressed as

$$\begin{cases} i_{md}^W = i_{md}^M \cos(\delta) - i_{mq}^M \sin(\delta) \\ i_{mq}^W = i_{md}^M \sin(\delta) + i_{mq}^M \cos(\delta) \end{cases} \tag{19}$$

where i_{md}^M and i_{mq}^M are d- and q-axis components of the fault current from MMC in its own synchronous reference frame. When represented in the synchronous reference frame of wind turbine VSC, the d- and q-axis components of the fault current from MMC are expressed as i_{md}^W and i_{mq}^W.

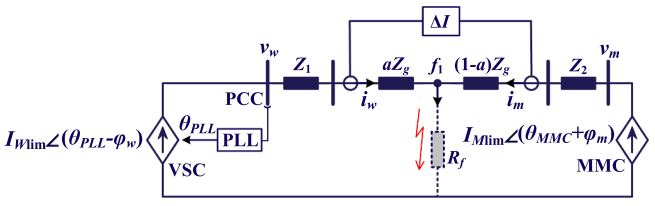

Fig. 11. Single-line diagram of MMC-connected OWF with symmetrical 3-phase-to-ground fault on the HV feeder.

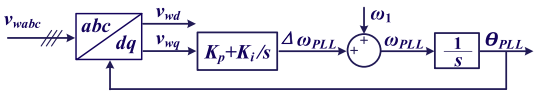

Fig. 12. Block diagram of the PLL.

After the onset of a symmetrical 3-phase-to-ground fault on the HV feeder with the fault resistance R_f as shown in Fig. 11, the PCC voltage of the wind turbine VSC can be expressed as:

$$v_w = i_w \left(Z_1 + aZ_g + R_f \right) + i_m R_f \tag{20}$$

where all the variables are expressed in the synchronous reference frame of wind turbine VSC.

Accordingly, the q-axis component v_{wq} of the PCC voltage of wind turbine VSC can be derived as

$$v_{wq} = i_{wd} X + i_{wq} R + I_{Mlim} R_f \sin(\varphi_m + \delta) \tag{21}$$

where

$$\begin{aligned} X &= \omega_1 \left(L_1 + aL_g \right) \\ R &= aR_g + R_f \end{aligned} \tag{22}$$

Based on the relationship of (21) and the block diagram of PLL as illustrated in Fig. 12, the equivalent diagram of the PLL after fault inception is shown as Fig. 13. Substituting equation (21) into (18), then applying the derivation to δ on both sides of equation (18) yields equation (23). The transient dynamics of the OWF-MMC system with the symmetrical 3-phase-to-ground fault can be characterized by (23), which is affected by the fault current phase angle φ_m of MMC.

$$\begin{aligned} \ddot{\delta} = & \frac{K_p I_{Mlim} R_f \cos(\varphi_m + \delta)}{-1 + K_p (aL_g + L_1) i_{wd}} \dot{\delta} + \frac{K_i}{-1 + K_p (aL_g + L_1) i_{wd}} \left[(aL_g + L_1) i_{wd} (\omega_1 \right. \\ & \left. - \dot{\delta}) + i_{wq} \left(aR_g + R_f \right) + I_{Mlim} R_f \sin(\varphi_m + \delta) \right] \end{aligned} \tag{23}$$

According to the transient dynamic model of (23), the waveforms of δ with different φ_m after the symmetrical 3-phase-to-ground fault are illustrated in Fig. 14(a). δ is shown to have slow dynamics within two fundamental cycles after fault inception. Besides, the phase difference ϕ_{diff} of the fault currents from MMC and wind farm has significant impact on the efficacy of current differential protection according to the analysis in section III. When MMC adopts the different value of φ_m, the waveforms of ϕ_{diff} are illustrated in Fig. 14(b). Since φ_m can be controlled with high flexibility, ϕ_{diff} could exceed the SPDR when φ_m is not properly controlled. For instance, when φ_m is>90° and the other system parameters are shown in Table 1, ϕ_{diff} will exceed the SPDR within 40 ms after fault inception. As a result, the current differential protection fails to trip when the controller of MMC adopts these randomly selected φ_m.

5. Proposed coordinated control method

5.1. Basic idea

According to the previous analysis, if ϕ_{diff} exceeds the SPDR, the current differential relay could fail to trip after fault inception. Since the phase angle φ_w of the fault current from VSC follows the grid code, ϕ_{diff} is determined by the control of φ_m, which has significant impact on the efficacy of current differential protection. Therefore, a coordinated control method of MMC with the current differential protection is

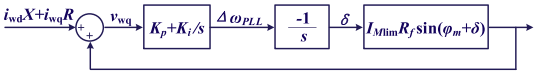

Fig. 13. Equivalent diagram of the PLL after fault inception.

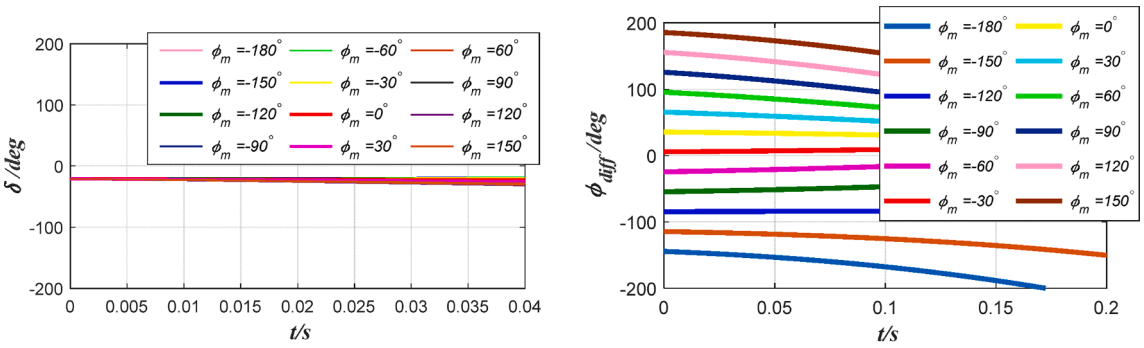

(a) The effect of φ_m on δ (b) The effect of φ_m on ϕ_{diff}

Fig. 14. The effect of φ_m on ϕ_{diff} and δ with the symmetrical 3-phase-to-ground fault (R_f = 40 Ω) on the HV feeder.

Table 1
Main system parameters.

Symbol	Meaning	Values
P	Power rating of the offshore wind farm	100 MW
V_m	RMS value of the rated ac voltage of MMC	210 kV
f_1	Nominal grid frequency	50 kH
V_w	RMS value of the rated ac voltage of wind turbine VSC	0.69 kV
I_{lim}	The limit value of the current from converters	1.2p.u.
X_{tr}	The leakage reactance of transformers	0.12p.u.

proposed in this part to improve the efficacy of protection relay in the OWF-MMC system.

The core idea of the proposed coordinated control with the current differential protection is trying to align the fault current i_m from MMC with the fault current i_w from wind farm. As a result, the controlled fault current of MMC according to the proposed method can make the fault currents of OWF-MMC system to mimic the SGs dominated system, where the phase angle of the fault currents from both sides of the faulty line are very close. As illustrated in Fig. 15, the increase of ϕ_{diff} will lead to the decrease of the differential current $\left|\dot{I}_m + \dot{I}_w\right|$, and further lead to the failure of the current differential protection. On contrary, the aligned fault currents can provide the largest differential current ensuring the trip of the relay after fault inception.

5.2. The proposed coordination method

In order to align the fault current i_m from MMC with the fault current i_w from wind farm, $\varphi_m = -\delta - \varphi_w$ should be satisfied for the proposed method according to (3). After fault inception, the phase angle φ_w of the fault current from wind turbine VSC is determined by the PCC voltage v_w according to the grid code, which is a function of the terminal voltage and can be expressed as

$$\varphi_w = f_{FRT\_VSC}(v_w) \tag{24}$$

Different from φ_w, the phase angle φ_m of the fault current from MMC can be controlled with high flexibility since there are no grid codes on it. Considering φ_m is the unused control freedom of the MMC, the coordinated control of φ_m with the current differential protection does not contradict with existing control objectives of the OWF-MMC system. Besides, the proposed coordinated control does not require any modifications on the traditional current differential protection algorithm, which simplifies the field implementation.

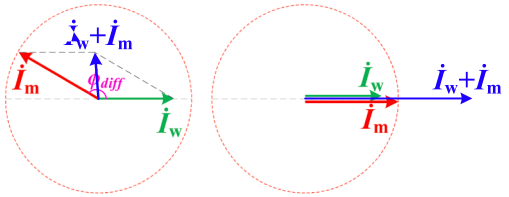

Fig. 15. The core idea of the proposed method.

The equivalent diagram of the OWF-MMC system during normal operation is shown in Fig. 16. Accordingly, the power angle before fault inception can be expressed as

$$\delta_{prefault} = -\arcsin\left(\frac{2P\omega_1 L_{eq}}{3v_w v_m}\right) \tag{25}$$

where P is the transferred active power from wind farm to MMC, L_{eq} represents the sum of the transformer leakage inductance and the line inductance. Since δ varies slowly within two fundamental cycles after fault inception as shown in Fig. 14(a), $\delta_{prefault}$ can be utilized to replace δ when calculating φ_m in the proposed coordination method.

Therefore, φ_m should be controlled to satisfy (26) in order to align the fault current i_m from MMC with the fault current i_w from wind farm. However, it is hard for MMC to access the PCC voltage v_w of the OWF. Since the equivalent inductance L_{eq} of Fig. 16 is not very large in practical applications, the terminal voltage v_m of MMC has the similar per-unit (p.u.) value with v_w, and therefore can be utilized to replace v_w when calculating φ_m as shown in (26). The worst-case study will validate that this replacement is feasible even when v_m significantly deviates from v_w.

$$\begin{aligned}\varphi_m &= -f_{FRT\_VSC}(v_w) - \delta_{prefault} \\ &\approx -f_{FRT\_VSC}(v_m) - \delta_{prefault}\end{aligned} \tag{26}$$

According to the calculated phase angle φ_m of the fault current from MMC as expressed in (26), the proposed reactive current response of MMC is illustrated as the red line of Fig. 17. The dashed blue line is the grid code for wind turbine VSC on low-voltage ride-through after fault inception. The injected active current of converters can be calculated according to (2).

5.3. Robustness analysis

To check the impact of the proposed response of MMC on the efficacy of current differential protection, the phase difference ϕ_{diff} of the fault currents from VSC and MMC with different fault resistance is illustrated in Fig. 18. Since a lot of factors, i.e., human activity, environmental factors, and manufacturing errors, could lead to the cable fault, a wide

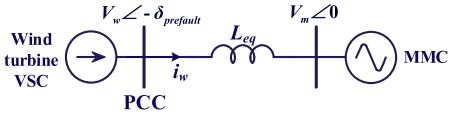

Fig. 16. The equivalent diagram of the HVDC-connected OWF during normal operation.

range of fault resistance is investigated. It is shown that the proposed response of MMC can ensure ϕ_{diff} is within the SPDR with low- and high-impedance short circuit fault.

Theoretically, the proposed method can make sure i_m is aligned with i_w if the controller of MMC has access to the terminal voltage of VSC. Since the terminal voltage of MMC is used to replace that of the VSC in the proposed method to avoid the communication delay and the investment cost [26], there could be the phase difference between i_m and i_w in some cases. Therefore, it is necessary to find the worst case to check the theoretical maximum phase difference between i_m and i_w after applying the proposed coordination method. Although it cannot happen in most practical applications, the worst-case is when the PCC voltage v_w of VSC is>0.9p.u. ($\varphi_w = 0$) and the PCC voltage v_m of MMC is<0.5p.u. as shown in Fig. 19. In the worst-case, the maximum phase difference between i_m and i_w can be calculated as expressed in (27). Since the maximum phase difference in the worst case is within the SPDR, it validates that the proposed coordinated control of MMC can guarantee the reliable operation of current differential protection after fault inception even with the maximum phase difference between i_m and i_w that rarely exists in practical applications.

$$\begin{aligned}\phi_{diff\_worst} &= \varphi_m + \delta + \varphi_w \\ &= -f_{FRT\_VSC}(v_w) - \delta_{prefault} + \delta + \varphi_w \\ &\approx -f_{FRT\_VSC}(v_m) + f_{FRT\_VSC}(v_w) \\ &\approx -56^\circ\end{aligned} \tag{27}$$

6. Simulations

To validate the proposed coordinated control of MMC with the current differential protection, EMT simulations of the HVDC-connected OWF are conducted considering the different fault locations, fault resistance, control schemes, and the different system structures.

6.1. Busbar protection

6.1.1. Busbar protection when adopting the coordinated control (case 1)

After the inception of a symmetrical 3-phase-to-ground fault (R_f = 40 Ω) on busbar in the OWF with two clusters as illustrated in Fig. 7, the EMT simulation results are given in Fig. 20. The parameters of the two clusters are assumed to be the same for simplicity. Since the coordinated control is applied, the fault current of MMC is aligned with that of the wind farm clusters after fault inception at 3 s as shown in Fig. 20(a). Besides, the restraint current I_{res} and the differential current I_{op} of the current differential relay for busbar is illustrated in Fig. 20(b). The trajectory of I_{res} and I_{op} is plotted in Fig. 20(c) as the red line, which crosses the relay operating characteristic 12 ms after fault inception and the relay trips accordingly.

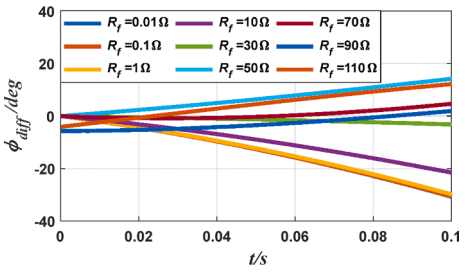

Fig. 18. The effect of fault resistance R_f on ϕ_{diff} with the proposed coordinated control method.

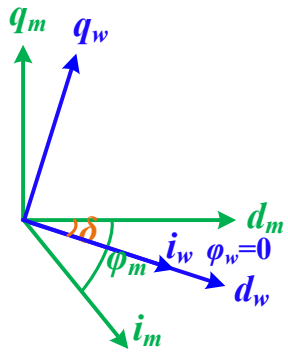

Fig. 19. The maximum phase difference between i_m and i_w in the worst-case.

6.1.2. Busbar protection without the coordinated control (case 2)

When the coordinated control is not implemented and φ_m takes a randomly selected value, e.g. 120°, the simulation results of the OWF-MMC system are shown in Fig. 21 after the onset of a symmetrical 3-phase-to-ground fault (R_f = 40 Ω) on busbar at 3 s. It is obvious that the fault current of MMC is no longer aligned with that of the wind turbine VSC. Besides, it takes 210 ms for the trajectory of I_{res} and I_{op} to cross the relay operating characteristic and trip the current differential relay, which means the speed of the relay declines severely.

6.2. Feeder protection

6.2.1. OWF with two HV feeders and adopting the coordinated control (case 3)

After the inception of a symmetrical 3-phase-to-ground fault (R_f = 40 Ω) on HV feeder 1 in the OWF with two HV feeders, the EMT simulation results are shown in Fig. 22. The phase angle of the fault current i_m from MMC follows the proposed coordinated control method. Therefore,

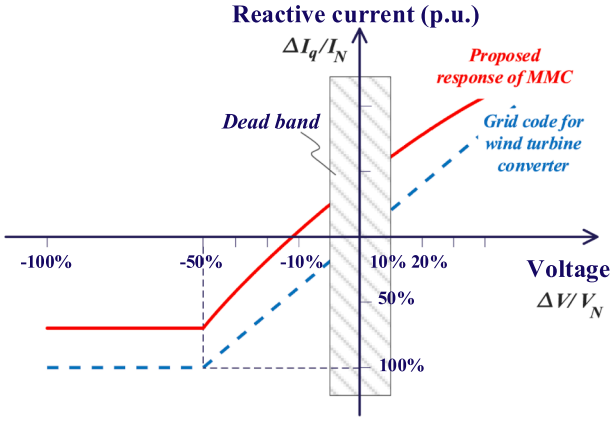

Fig. 17. The proposed response of MMC.

i_m is aligned with i_w after fault inception at 3 s as shown in Fig. 22 (a). The current differential protection for HV feeder 1 utilizes the fault currents information of both sides of the feeder to detect the fault condition. As illustrated in Fig. 9, the fault currents of both sides of HV feeder 1 are i_{sum} and i_{w1}, respectively. The waveforms of i_{sum} and i_{w1} are shown in Fig. 22 (b), where they are aligned with each other after fault inception. Besides, the trajectory of I_{op} and I_{res} is given in Fig. 22 (d). Ten milliseconds after fault inception, the trajectory crosses the relay operation characteristic and then the relay can successfully trip.

6.2.2. OWF with eight HV feeders and adopting the coordinated control (case 4)

When the number of HV feeders increases to eight, the EMT simulation results are shown in Fig. 23. MMC adopts the proposed coordinated control with the current differential protection. As a result, i_{w1} is aligned with i_m and i_{sum} after fault inception on HV feeder 1. Since there are eight identical wind farm clusters connected with MMC, i_{sum} is the sum of the fault currents from MMC and the other seven healthy feeders as illustrated in Fig. 23(b). Besides, Fig. 23(d) shows the trajectory of I_{op} and I_{res}, which quickly crosses the relay operating characteristic within 3 ms after fault inception and the relay trips correspondingly.

6.2.3. OWF-MMC system without coordinated control (case 5)

When the proposed coordinated control is not applied, the EMT simulation of the symmetrical 3-phase-to-ground fault (R_f = 40 Ω) on HV feeder 1 in the OWF with two HV feeders is shown in Fig. 24. After fault inception, the phase angle of the fault current from MMC is randomly selected as $\varphi_m = 120°$. In this case, i_{w1} is no longer aligned with i_m and i_{sum} after the fault inception. Besides, the trajectory of I_{op} and I_{res} will not cross the relay operating characteristic until 150 ms after fault inception. Although the current differential relay can finally trip, the speed is compromised.

6.2.4. OWF-MMC system adopting the coordinated control with different fault resistance (case 6)

To validate the applicability of the proposed method to the different fault resistance, the EMT simulation of the symmetrical 3-phase-to-ground fault on HV feeder 1 with fault resistance R_f = 0.01 Ω is shown in Fig. 25. The OWF is connected to the MMC station through two HV feeders. Since MMC adopts the proposed coordinated control with the current differential protection, i_{w1} can get aligned with i_m and i_{sum} within two fundamental cycles after fault inception. Besides, Fig. 25 (d) shows that the trajectory of I_{op} and I_{res} crosses the relay operating characteristic 7 ms after fault inception. Therefore, the current differential protection can successfully trip even with the severe low impedance short-circuit fault when adopting the proposed coordinated control method.

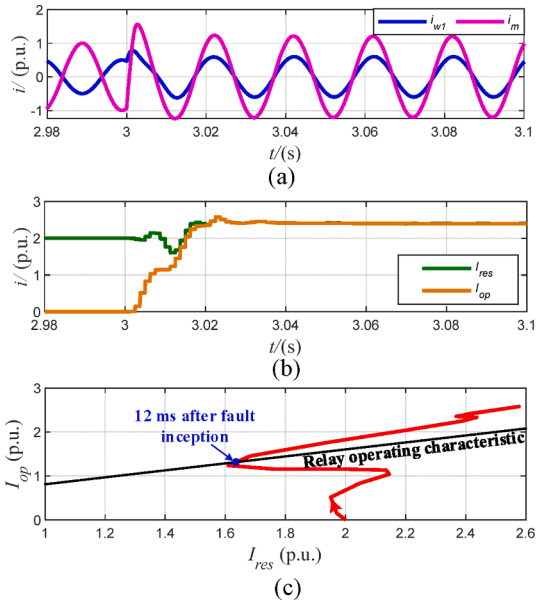

Fig. 20. EMT simulation of the symmetrical 3-phase-to-ground fault (R_f = 40 Ω) on busbar when the coordinated of MMC is applied.

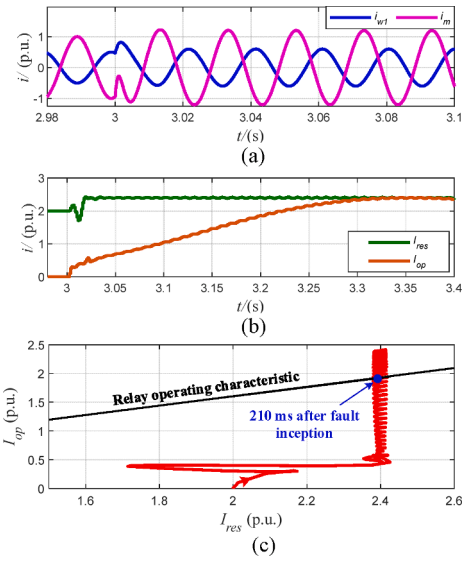

Fig. 21. EMT simulation of the symmetrical 3-phase-to-ground fault (R_f = 40 Ω) on busbar when the coordinated control is not applied ($\varphi_m = 120°$).

7. RTDS verification

To further validate the proposed coordinated control of MMC with the current differential protection in the HVDC-connected OWF, the experimental setup based on RTDS is built as illustrated in Fig. 26. The experimental setup mainly consists of two RTDS racks, an Ethernet switch, and a workstation. The OWF-MMC system is established and compiled on the RSCAD platform of the workstation, then executed in the RTDS hardware. The RunTime module of RSCAD can communicate and control in real time with the PB5 processor cards of the RTDS racks through the Ethernet switch and the GTWIF (Giga Transceiver Workstation InterFace) card [27]. The sampled real-time fault currents are compared with the operation characteristics of the current differential relay, then the trip signal is generated in the event of a short-circuit fault.

The recorded real-time fault data are utilized for the protection evaluation as shown in Fig. 27. The six fault cases and the response of current differential protection as presented in section VI are verified. The short-circuit faults are applied at zero second and the corresponding ratios of the differential current and restraint current of the current differential protection for different cases are illustrated in Fig. 27. When the ratio of the differential current and restraint current I_{op}/I_{res} is greater than the setting value 0.8, the relay will trip according to the operation criteria of (7). The waveforms of I_{op}/I_{res} for different cases are consistent with the analysis of section VI, which further validates the proposed coordinated fault current control of MMC in HVDC-connected offshore wind farm with the current differential protection.

8. Conclusion

This paper proposed the coordinated control of MMC with the current differential protection in the HVDC-connected OWF. It is revealed that the phase difference φ_{diff} of the fault currents between MMC and wind turbine VSC has significant impact on the efficacy of current

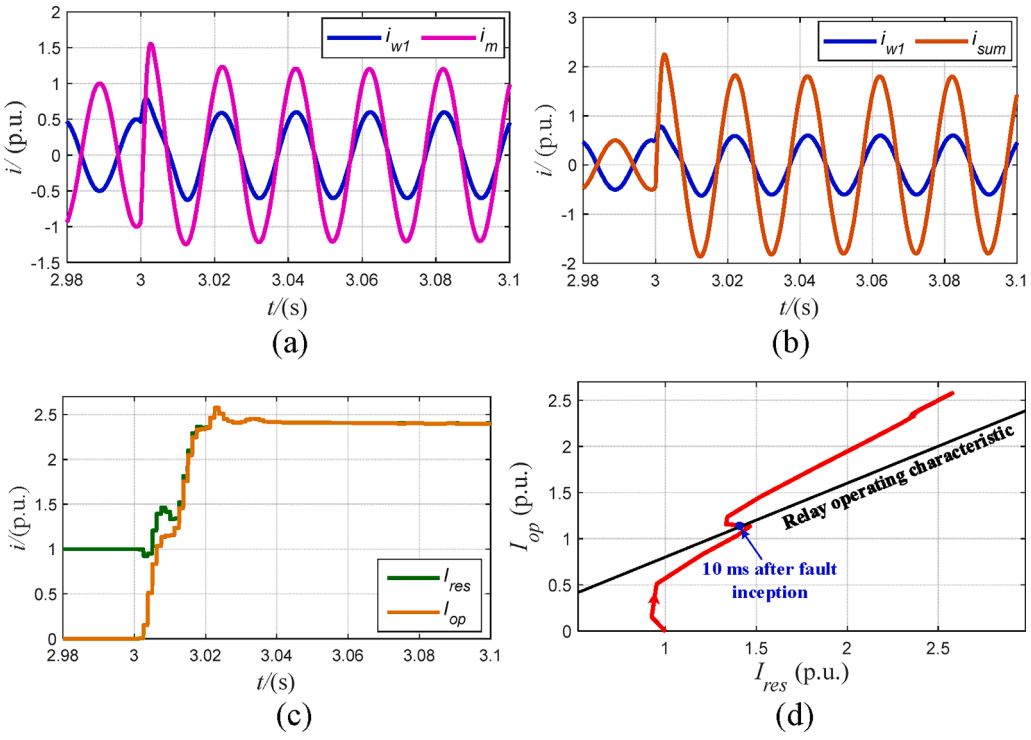

Fig. 22. EMT simulation of the symmetrical 3-phase-to-ground fault ($R_f = 40\ \Omega$) on HV feeder 1 in the OWF with two HV feeders.

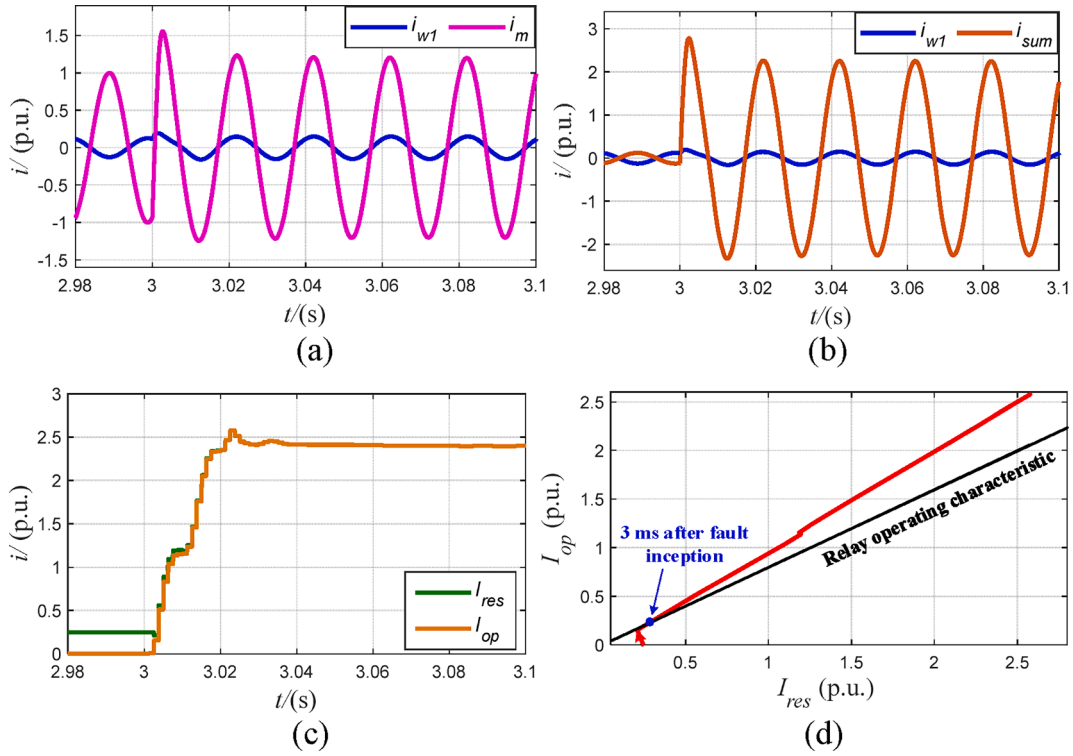

Fig. 23. EMT simulation of the symmetrical 3-phase-to-ground fault ($R_f = 40\ \Omega$) on HV feeder 1 in the OWF with eight HV feeders.

differential protection. Since the phase angle of the fault current from VSC follows the grid code, φ_{diff} is determined by the control of MMC. Therefore, the coordinated control of the fault current from MMC with the current differential protection is proposed. It is illustrated that the coordinated control can improve the efficacy of current differential protection by aligning the fault current of MMC with that of the VSC. Finally, the EMT simulation results in PSCAD and the real-time digital simulator (RTDS) are given to verify the theoretical analysis.

CRediT authorship contribution statement

Guoqing Gao: Conceptualization, Methodology, Software,

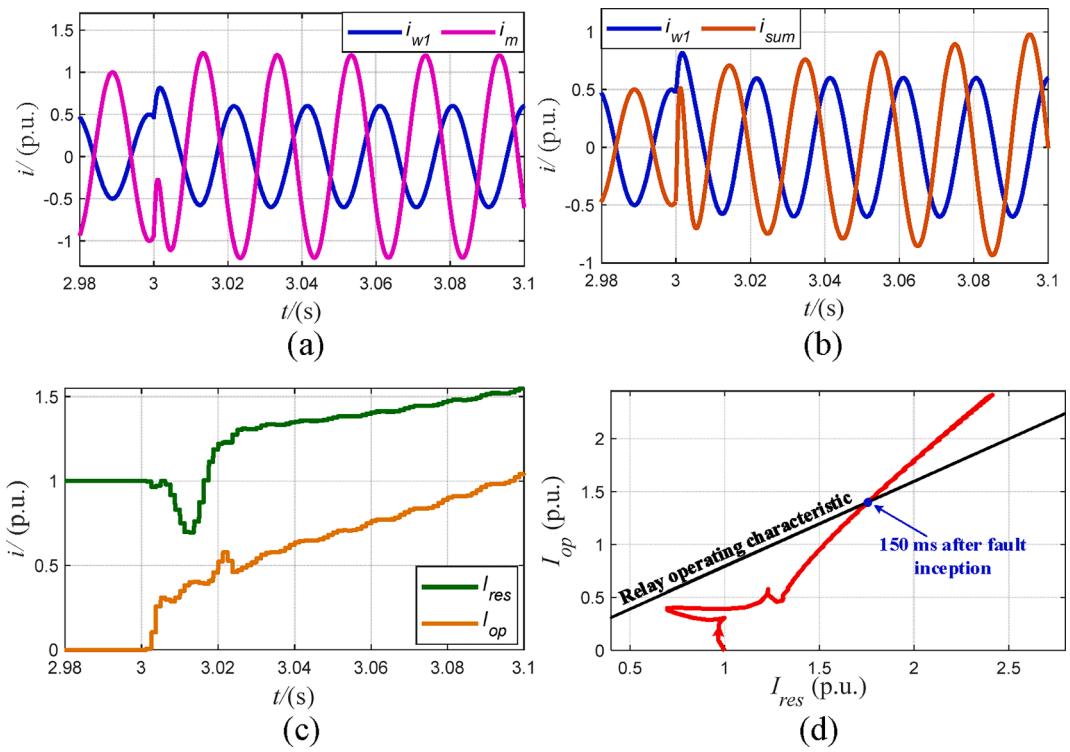

Fig. 24. EMT simulation of the symmetrical 3-phase-to-ground fault ($R_f = 40\ \Omega$) on HV feeder 1 in the OWF with two HV feeders when the coordinated control is not applied ($\varphi_m = 120°$).

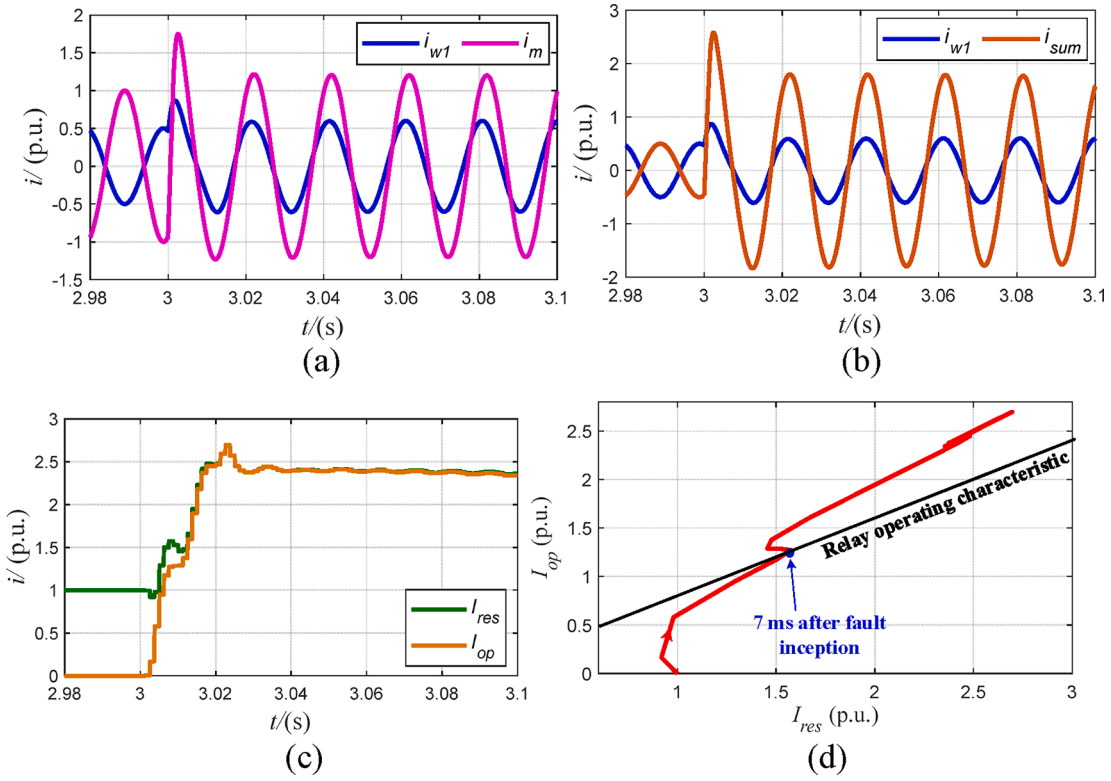

Fig. 25. EMT simulation of the symmetrical 3-phase-to-ground fault ($R_f = 0.01\ \Omega$) on HV feeder 1 in the OWF with two HV feeders.

Validation, Writing – original draft. **Heng Wu:** Supervision, Writing – review & editing, Software. **Frede Blaabjerg:** Supervision, Writing – review & editing. **Xiongfei Wang:** Supervision, Writing – review & editing, Project administration.

Declaration of Competing Interest

The authors declare that they have no known competing financial interests or personal relationships that could have appeared to influence

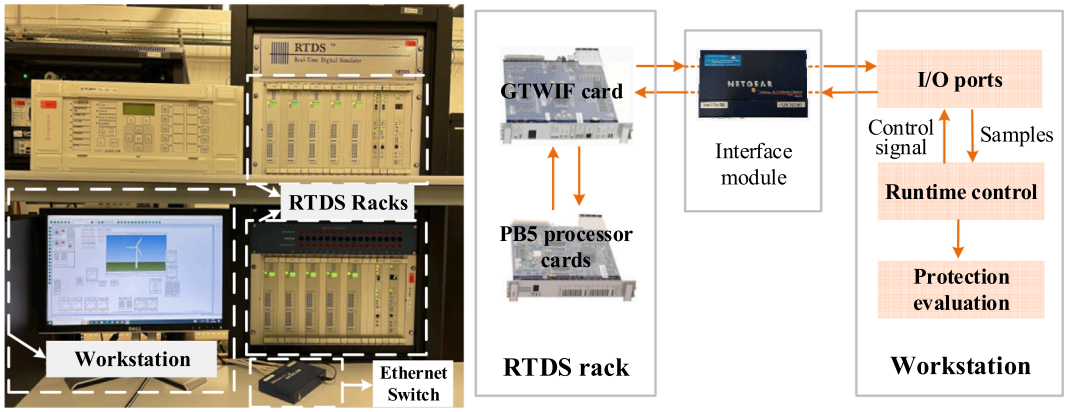

(a) Field configuration (b) Simplified diagram of the setup

Fig. 26. The experimental setup based on RTDS.

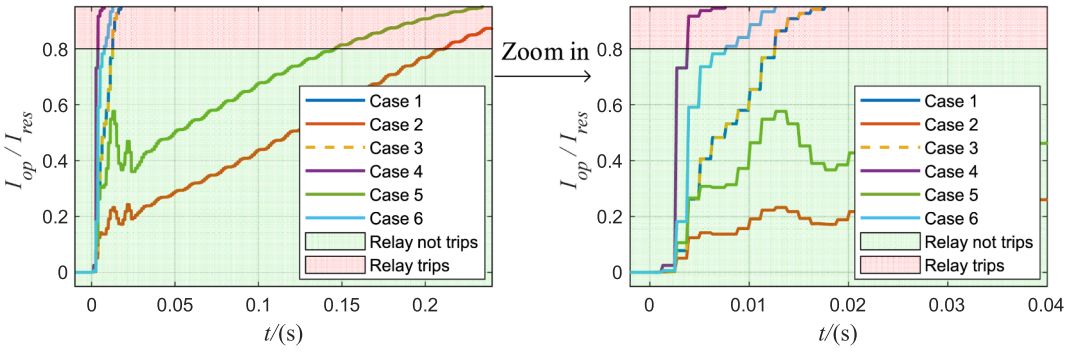

Fig. 27. The ratios of the differential current and restraint current of the current differential protection for different cases.

the work reported in this paper.

Data availability

No data was used for the research described in the article.

Acknowledgements

This work is funded by the European Union's Horizon 2020 Research and Innovation Program under the Marie Sklodowska-Curie grant agreement No 861398.

References

[1] Yaramasu V, Wu B, Sen PC, Kouro S, Narimani M. High-power wind energy conversion systems: State-of-the-art and emerging technologies. Proceedings of the IEEE. 2015;103:740-88.
[2] Gao G, Wu H, Wang X. Converter Control Impacts on Efficacy of Protection Relays in HVDC-Connected Offshore Wind Farms. In: 2022 IEEE 13th International Symposium on Power Electronics for Distributed Generation Systems. (PEDG): IEEE; 2022. p. 1–6.
[3] Li YW, Vilathgamuwa DM, Loh PC. Blaabjerg FJItope. A dual-functional medium voltage level DVR to limit downstream fault currents 2007;22:1330–40.
[4] Korompili A, Wu Q, Zhao HJR, Reviews SE. Review of VSC HVDC connection for offshore wind power integration 2016;59:1405–14.
[5] Erlich I, Bachmann U. Grid code requirements concerning connection and operation of wind turbines in Germany. IEEE Power Engineering Society General Meeting 2005;2:1253–7.
[6] Haddadi A, Farantatos E, Kocar I, Karaagac U. Impact of Inverter Based Resources on System Protection. Energies 2021:14.
[7] Ziegler G. Numerical differential protection: principles and applications. John Wiley & Sons; 2012.
[8] Liang Y, Li W, Xu G. Performance Problem of Current Differential Protection of Lines Emanating from Photovoltaic Power Plants. Sustainability 2020:12.
[9] Prasad CD, Biswal M, Abdelaziz AY. Adaptive differential protection scheme for wind farm integrated power network. Electric Power Systems Research 2020;187:106452.
[10] Li Y, Jia K, Bi T, Yan R, Li W, Liu B. Analysis of line current differential protection considering inverter-interfaced renewable energy power plants. 2017 IEEE PES Innovative Smart Grid Technologies Conference Europe (ISGT-Europe)2017. p. 1-6.
[11] Muzzammel R. Traveling Waves-Based Method for Fault Estimation in HVDC Transmission System. Energies 2019:12.
[12] Khalili M, Namdari F, Rokrok E. A novel protection scheme for hybrid transmission systems connected to DFIG-based wind farms using game theory. IET Renew Power Gener 2021;15:2409–25.
[13] Zheng L, Jia K, Bi T, Fang Y, Yang Z. Cosine Similarity Based Line Protection for Large-Scale Wind Farms. IEEE Trans Ind Electron 2021;68:5990–9.
[14] Zheng L, Jia K, Wu W, Liu Q, Bi T, Yang Q. Cosine Similarity Based Line Protection for Large Scale Wind Farms Part II - the Industrial Application. IEEE Trans Ind Electron 2021:1 -.
[15] Jia K, Li Y, Fang Y, Zheng L, Bi T. Yang QJAe. Transient current similarity based protection for wind farm transmission lines 2018;225:42–51.
[16] Liang Y, Ren Y, He W. An Enhanced Current Differential Protection for AC Transmission Lines Connecting MMC-HVDC Stations. IEEE Syst J 2022;1–12.
[17] Jia K, Shi Z, Wang C, Li J, Bi T. Active Converter Injection-Based Protection for a Photovoltaic DC Distribution System. IEEE Trans Ind Electron 2022;69:5911–21.
[18] Song G, Hou J, Guo B, Hussain KST, Wang T, Masood B. Active Injection for Single-Ended Protection in DC Grid Using Hybrid MMC. IEEE Trans Power Delivery 2021;36:1651–62.
[19] Song G, Hou J, Guo B, Chen ZJP. Systems CoMP. Pilot protection of hybrid MMC DC grid based on active detection 2020;5:1–15.
[20] Li Y, Guo J, Wu H, Wang X, Zhao B, Wang S, et al. Voltage Stability and Transient Symmetrical Fault Current Control of Voltage-Controlled MMCs. IEEE Trans Power Delivery 2020;35:2506–16.
[21] Wang X, Wu H, Wang X, Dall L, Kwon JB. Dynamic Impact of Voltage-Dependent Current Injection on Fault-Ride-Through of Grid-Following Converters. 2021 IEEE Energy Conversion Congress and Exposition (ECCE)2021. p. 369-74.
[22] Graungaard Taul M, Wang X, Davari P, Blaabjerg F. Current Reference Generation Based on Next-Generation Grid Code Requirements of Grid-Tied Converters During Asymmetrical Faults. IEEE Journal of Emerging and Selected Topics in Power Electronics 2020;8:3784–97.
[23] Li Y, Wang X, Jianbo G, Wu H, Zhao B, Wang S, et al. PLL Synchronization Stability Analysis of MMC-Connected Wind Farms under High-Impedance AC Faults. IEEE Trans Power Syst 2020:1 -.
[24] Erlich I, Shewarega F, Feltes C, Koch FW. Fortmann JJPotI. Offshore wind power generation technologies 2013;101:891–905.

[25] Wu H, Wang X. Design-Oriented Transient Stability Analysis of PLL-Synchronized Voltage-Source Converters. IEEE Trans Power Electron 2020;35:3573–89.
[26] Vidal-Albalate R, Beltran H, Rolan A, Belenguer E, Pena R, Blasco-Gimenez R. Analysis of the Performance of MMC Under Fault Conditions in HVDC-Based Offshore Wind Farms. IEEE Trans Power Delivery 2016;31:839–47.
[27] Yang Z, Liao W, Zhang Q, Leth Bak C, Chen Z. Fault Coordination Control for Converter-interfaced Sources Compatible with Distance Protection during Asymmetrical Faults. IEEE Trans Ind Electron 2022;1–11.